

Double-Shot 3D Shape Measurement with a Dual-Branch Network

Mingyang Lei, Jingfan Fan*, Long Shao, Hong Song, Deqiang Xiao, Danni Ai, Tianyu Fu, Ying Gu*, and Jian Yang*

Abstract—The structured light (SL)-based 3D measurement techniques with deep learning have been widely studied, among which speckle projection profilometry (SPP) and fringe projection profilometry (FPP) are two popular methods. However, they generally use a single projection pattern for reconstruction, resulting in fringe order ambiguity or poor reconstruction accuracy. To alleviate these problems, we propose a parallel dual-branch Convolutional Neural Network (CNN)-Transformer network (PDCNet), to take advantage of convolutional operations and self-attention mechanisms for processing different SL modalities. Within PDCNet, a Transformer branch is used to capture global perception in the fringe images, while a CNN branch is designed to collect local details in the speckle images. To fully integrate complementary features, we design a double-stream attention aggregation module (DAAM) that consist of a parallel attention subnetwork for aggregating multi-scale spatial structure information. This module can dynamically retain local and global representations to the maximum extent. Moreover, an adaptive mixture density head with bimodal Gaussian distribution is proposed for learning a representation that is precise near discontinuities. Compared to the standard disparity regression strategy, this adaptive mixture head can effectively improves performance at object boundaries. Extensive experiments demonstrate that our method can reduce fringe order ambiguity while producing high-accuracy results on a self-made dataset. We also show that the proposed architecture reveals the potential in infrared-visible image fusion task.

Index Terms—Dual-Branch Framework, Attention Mechanism, Structured-Light Projection Profilometry, Deep Learning

I. INTRODUCTION

OPTICAL 3D measurement based on structured light projection has become a popular non-contact 3D shape measurement technique. It is a core problem for many vision tasks and has numerous applications such as

This work was supported in part by the National Key Research and Development Program of China under Grant 2023YFC2415300 and National Science Foundation Program of China under Grant 62025104 and Grant U22A2052. (Corresponding author: Jingfan Fan, Ying Gu, and Jian Yang).

Mingyang Lei, Tianyu Fu and Ying Gu are with the School of Medical Technology, Beijing Institute of Technology, Beijing 100081, China (e-mail: 13120030055@163.com; fty0718@bit.edu.cn; guyinglaser301@163.com).

Long Shao and Hong Song is with the School of Computer Science and Technology, Beijing Institute of Technology, Beijing 100081, China (e-mail: songhong@bit.edu.cn).

Jingfan Fan, Deqiang Xiao, Danni Ai, and Jian Yang are with the Beijing Engineering Research Center of Mixed Reality and Advanced Display, School of Optics and Photonics, Beijing Institute of Technology, Beijing 100081, China (e-mail: fjf@bit.edu.cn; xiaodq2011@gmail.com; dannai@bit.edu.cn; jyang@bit.edu.cn).

robotic sensing, product inspection, and biometric identification [1]. Due to the powerful representative capability of deep learning for various vision tasks [2], it has been employed to improve the structured light (SL)-based measurement performance and outperforms traditional methods significantly [3]. Among these algorithms, fringe projection profilometry (FPP) based on sinusoidal fringe patterns, and speckle projection profilometry (SPP) based on speckle patterns are two popular methods. However, they are all single-shot-based methods [4-6], which use a fringe or a speckle image as input and may cause errors in actual measurements. To be specific, FPP methods generally obtain the 3D measurement results from a few fringe patterns. Due to the continuity and periodicity nature of sinusoidal patterns, determining accurate fringe order with global information is the key to pixel-wise phase measurement. However, in some occluded scenes, the change in depth may lead to ambiguity in the fringe order. The order of the fringes projected on two objects is difficult to judge. As for the SPP methods, the speckle images modulated by the object surface is captured by the camera and then utilized to obtain the depth maps with various networks. However, SPP technology does not employ pixel-by-pixel encoding [7]. Instead, it mainly encodes the feature information within the local speckle regions, lacking pixel-wise global information like that within the fringe image, which may obtain poor results. For a monocular SL system, the change in depth will bring about the movement of the speckle spots, but the distribution pattern of these spots remains unchanged. Therefore, the local information within the speckle images is the most significant clue for 3D measurement.

To fully leverage the advantages of these methods and alleviate the aforementioned problems in SL-based 3D measurement tasks, we propose a dual-branch Convolutional Neural Network (CNN)-Transformer framework for recovering accurate 3D shapes (Fig 1(d)). Within the proposed double-shot-based method, we use the convolution operators to extract local features from speckle images and the self-attention mechanisms to capture global representations from fringe images. The main contributions of our paper are as follows:

- Considering the complementarity of the fringe and the speckle images, we feed them into separate Transformer and CNN branches to capture global perception and local details respectively. Especially in the fringe ambiguity regions, the distribution invariance of speckles helps PDCNet to achieve excellent measurement performance.
- We propose a double-stream attention aggregation module (DAAM) to integrate complementary features, which can aggregate multi-scale structure information. Especially in

the occluded scenes, DAAM pays more attention to crucial information compared to other attention modules.

- For recovering sharp boundaries, we exploit a novel bimodal Gaussian distribution with disparity adaptive selection strategy, to learn a representation that is precise near discontinuities.

We validate the effectiveness of the proposed method on a self-made dataset, which consists of occluded scenes and non-occluded scenes. The experimental results demonstrate that our method exhibits the lowest measurement error compared to other state-of-the-art methods.

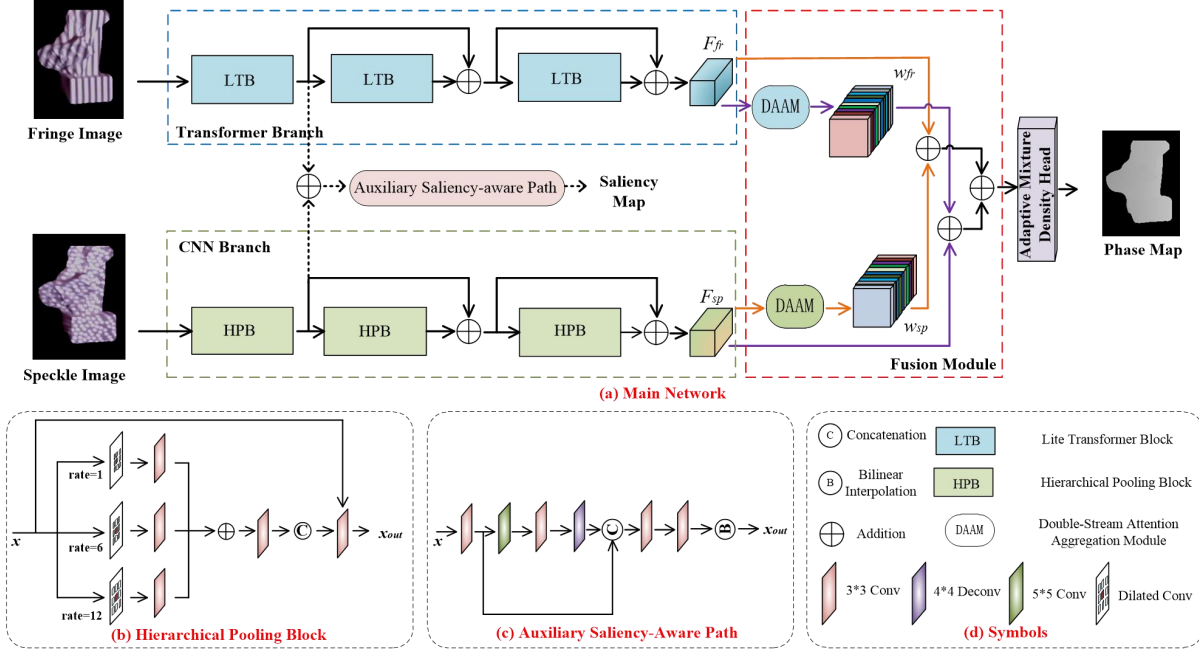


Fig. 1. The architecture of our PDCNet.

III. METHOD

A. Network Structure

In CNN, the convolution operations are good at extracting local features but difficult to capture global representations. In contrast, in Transformer, cascading attention mechanisms can model long-range dependencies, but break local feature details. To solve these problems, we propose a novel framework to take advantage of convolutional operations and self-attention modules for enhancing the representation learning of speckle images and fringe images respectively (Fig. 1).

B. CNN Branch

The CNN branch consists of three hierarchical pooling blocks (HPB) for effective incorporation of context. The HPB (Fig. 3(b)) first uses dilation convolution with different dilation rates and a 3×3 convolution layer to form a pyramid feature, which can enlarge the receptive fields with high efficiency. Then, we add up the obtained features of different branches, and a convolution layer is followed to get the aggregated feature map. Finally, a dense connection is used for generating the final

output feature map x_{out} , which has a regularizing effect and can reduce overfitting on the phase measurement task. The final output feature map can be summarized as:

$$x_{out} = f^{3 \times 3}([f^{3 \times 3}(f^{3 \times 3}(r_1(x)) \oplus f^{3 \times 3}(r_6(x)) \oplus f^{3 \times 3}(r_{12}(x))); x]) \quad (1)$$

where r_i represents the convolution kernel with dilation factor i . $f^{3 \times 3}$ denotes a convolution operation with a filter size of 3×3 .

C. Transformer Branch

The Transformer branch contains two stages: Pre-feature extraction and Main feature extraction. The previous work by Tete et al. [25] demonstrated that convolution is suitable for early visual processing. Therefore, we use a 3×3 convolution layer ($H_{pre}(\cdot)$) for this stage:

$$F_{pre} = H_{pre}(I_{fr}) \quad (2)$$

Then, the main feature is extracted from F_{pre} :

$$F_{main} = H_{main}(F_{pre}) \quad (3)$$

Considering to balance the performance and computational efficiency, we use three Lite Transformer blocks (LTB) [26] as the basic unit ($H_{main}(\cdot)$), which shrinks the embedding size to reduce the total computation amount while maintaining the same performance.

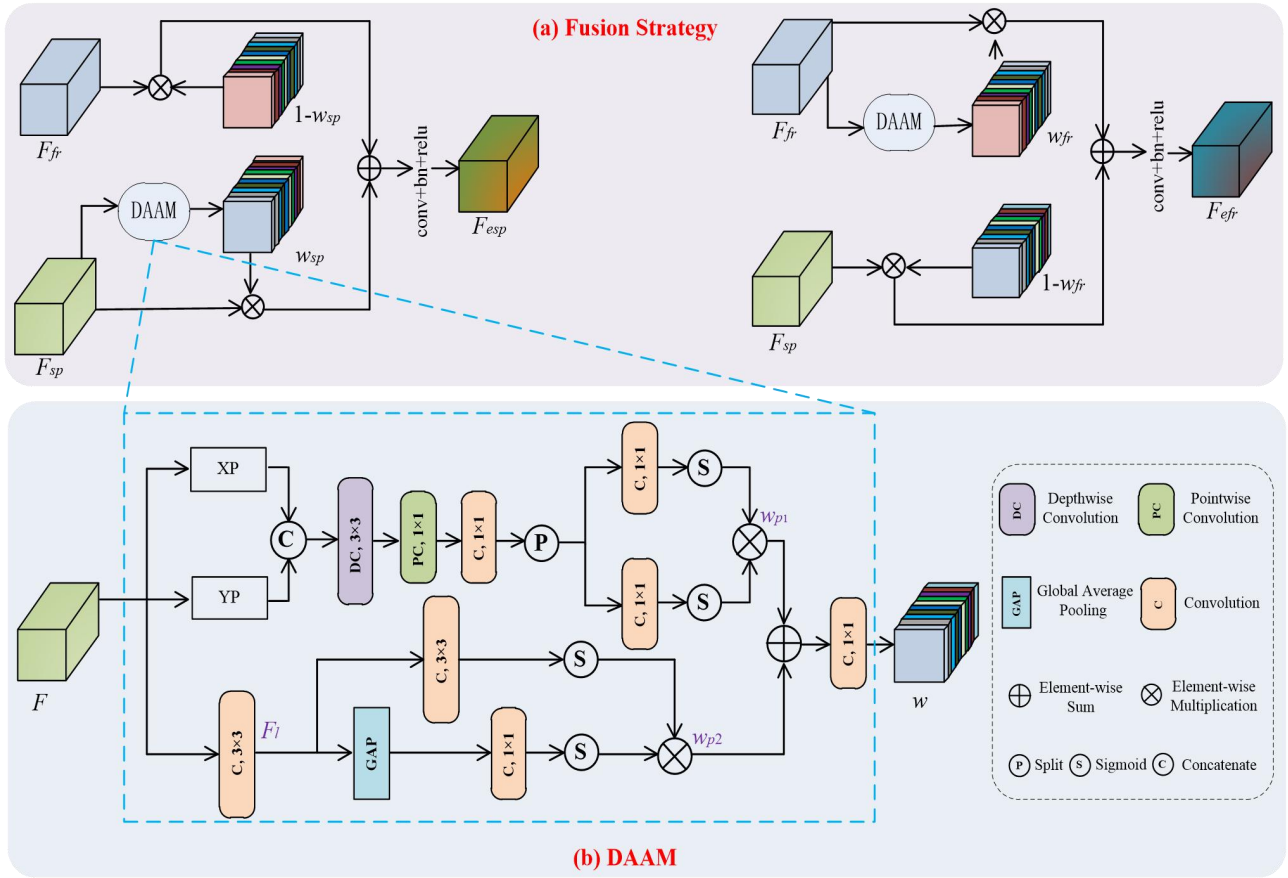


Fig. 2. The proposed fusion strategy and detailed structure of DAAM. ‘XP’ and ‘YP’ denote 1D horizontal global pooling and 1D vertical global pooling, respectively.

D. Auxiliary saliency-aware path

It has been verified by previous works [27, 28] that a proper auxiliary constraint path is beneficial to boosting the performance of different tasks. Moreover, similar tasks can reinforce each other, such as depth maps and semantic labels [29], which are pixel-level tasks and highly correlated with each other. Therefore, to improve the semantic characteristic of the output phase map, the saliency map and the phase map are simultaneously predicted in our proposed framework.

In our method, we use an auxiliary saliency-aware path (Fig. 3(c)) for enhancing the performance of shape measurement, which allows our network to be more focused on the object regions. Note that the auxiliary path only exists during the training stage, whereas it is abandoned when inference.

E. Fusion Strategy

Fig. 4(a) shows the specific structure of our cross-modal fusion strategy. Two weight matrices generated from F_{sp} and F_{fr} are multiplied with the input, to pay more attention to the important information and suppress the redundant features:

$$F_{esp} = F_{sp} * w_{sp} + F_{fr} * (1 - w_{sp}) \quad (4)$$

$$F_{efr} = F_{fr} * w_{fr} + F_{sp} * (1 - w_{fr}) \quad (5)$$

Then, these results are further added to generate the cross-modal feature F_{cm} :

$$F_{cm} = F_{esp} + F_{efr} \quad (6)$$

In this paper, we propose a novel double-stream attention aggregation module (DAAM) to obtain the weight matrix. Figure 4(b) presents the architecture of DAAM. Motivated by coordinate attention [30], we propose a parallel attention subnetwork for aggregating multi-scale spatial structure information.

Given a feature map F , a one-dimensional feature-encoding operation is performed on each channel using pooling kernels of size $(H, 1)$ and $(1, W)$ along the horizontal coordinate and the vertical coordinate, respectively. Next, these two maps are concatenated into F_{cat} so that they can share a convolution layer to keep the module as lightweight as possible.

$$F_{cat} = [AvgPool_h(F); AvgPool_w(F)] \quad (7)$$

The depthwise separable convolution (a depthwise convolution $Dconv(\cdot)$ followed by a pointwise convolution $Pconv(\cdot)$) [31] is adopted to encode spatial position information of F_{cat} .

$$F_h, F_w = Split[f^{1 \times 1}(PConv(Dconv(F_{cat}))) \quad (8)$$

For achieving different cross-channel interactive features between the two parallel paths, after dividing the outputs of 1×1 convolution into two vectors ($Split(\cdot)$), we aggregate the two channel-wise attention maps inside each group via a simple multiplication.

$$w_{p1} = \sigma(f^{1 \times 1}(F_h)) * \sigma(f^{1 \times 1}(F_w)) \quad (9)$$

where $\sigma(\cdot)$ is the sigmoid function. In addition, to aggregate multi-scale spatial structure information, a branch starts with a

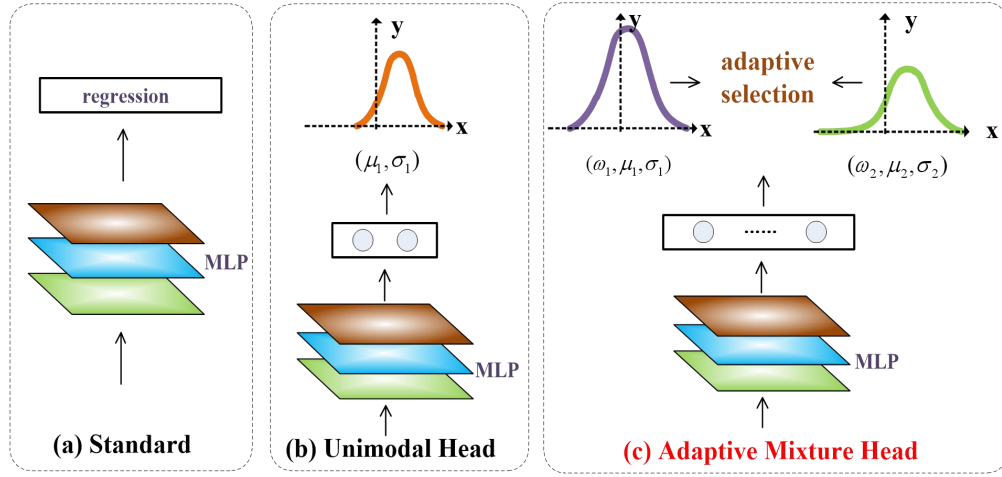


Fig. 3. Comparison of different prediction heads.

3×3 convolution is placed parallel to the above one. We perform global average pooling ($GAP(\cdot)$) and a 1×1 convolution for capturing more distinctive target information from a global perspective. Then, the obtained weights and the output of another 3×3 convolution path are multiplied as an attention weight matrix w_{p2} :

$$w_{p2} = \sigma(f^{1 \times 1}(GAP(F_1))) * \sigma(f^{3 \times 3}(F_1)) \quad (10)$$

Finally, we obtain the final output feature map through the channel-wise addition and a 1×1 convolution.

$$w = f^{1 \times 1}(w_{p1} + w_{p2}) \quad (11)$$

F. Adaptive Mixture Density Head

For obtaining sharp and precise disparity estimates near discontinuities, SMD-Nets [32] model the disparity using Laplacian distribution and exploit bimodal mixture densities as output representation. However, compared with Laplacian distribution, Gaussian distribution is widely used in various fields due to its convenient mathematical properties [33, 34]. Therefore, in this paper, we use bimodal Gaussian distribution with a novel disparity adaptive selection mechanism, to learn a representation that is precise at object boundaries (Fig. 5(c)).

To be specific, following SMD-Net [32], our backbone network ψ outputs a D -dimensional feature representation with a deterministic transformation:

$$\psi : \mathbb{R}^{W \times H \times 2} \rightarrow \mathbb{R}^D \quad (12)$$

where $D=96$, Note that the features are interpolated bilinear from its nearest four-pixel position for every continuous 2D location.

Next, we adopt a multi-layer perceptron Ω for mapping the

features to a five-dimensional vector $(\pi, \mu_1, \sigma_1, \mu_2, \sigma_2)$, which denotes the parameters of a bimodal Gaussian mixture distribution:

$$\Omega : \mathbb{R}^D \rightarrow \mathbb{R}^5 \quad (13)$$

The key issue then is to formulate the probability density, and this mixture distribution can be described as:

$$r(d) = \sum_{m=1}^M \omega_m \varphi_m(d) \quad (14)$$

where $M=2$ denotes a hyper-parameter denoting the number of components constituting the mixture model. ω_m represents the mixing coefficient which indicates the probability of different components. φ_m denotes the probability density function of component m . In this paper, we implement the Gaussian kernel into our framework:

$$\varphi_m(d) = \frac{1}{\sigma_m} e^{-\frac{(\mu_m - d)^2}{2\sigma_m^2}} \quad (15)$$

$$\omega_2 = 1 - \omega_1 \quad (16)$$

where σ_m indicates the common variance parameter, and μ_m denotes the mean of component m . By introducing two modes (μ_1, σ_1) , (μ_2, σ_2) in our method, we can obtain both the foreground and the background disparity near discontinuities (boundaries).

At the inference stage, a common strategy is to use the mode with the highest density value to estimate object boundaries. However, this is not robust in practice when the density values of the two modes are close [35]. Therefore, to overcome this problem, we propose a novel adaptive selection strategy. To be specific, we first obtain two candidate disparities by the mode with the highest density value and the lowest density value:

$$\hat{d}_{\max} = \arg \max_{d \in \{\mu_1, \mu_2\}} r(d) \quad (17)$$

$$\hat{d}_{\min} = \arg \min_{d \in \{\mu_1, \mu_2\}} r(d) \quad (18)$$

Then, if the density values corresponding to these two candidate disparities satisfy:

$$\frac{r(\hat{d}_{\max})}{r(\hat{d}_{\min})} < thr \quad (19)$$

we choose the average disparity value as the result. If Eq. 11 is not satisfied, we use \hat{d}_{\max} as the final disparity. In this paper, $thr=1.1$.

G. Loss Function

We train our base network by minimizing the negative log-likelihood loss:

$$L_N = -\log\left(\frac{\omega_1}{\sigma_1} e^{-\frac{(\mu_1-d)^2}{2\sigma_1^2}} + \frac{\omega_2}{\sigma_2} e^{-\frac{(\mu_2-d)^2}{2\sigma_2^2}}\right) \quad (20)$$

Moreover, for the auxiliary saliency-aware branch, binary cross-entropy loss is used as the loss function to measure the relation between the ground truth and the generated saliency map:

$$L_S = -\frac{1}{H \times W} \sum_{i=1}^H \sum_{j=1}^W [T_{ij} \log(P_{ij}) + (1-T_{ij}) \log(1-P_{ij})] \quad (21)$$

where H and W are the image's height and width, respectively. P_{ij} represents the probability associated with the presence of salient objects at position (i, j) . T_{ij} denotes the ground truth label assigned to the pixel (i, j) .

Overall, the total loss is given in Eq (22):

$$L_T = z_N L_N + (1-z_N) L_S \quad (22)$$

where z denotes the weight of different loss functions. In our experiments, $z_N=0.8$.

IV. EXPERIMENTS AND ANALYSIS

A. Dataset and Implementation Details

1) *Dataset*: We built a conventional projection profilometry system (Fig. 6) consisting of an industrial camera (640×480) and a DLP projector (LightCrafter 4500). The raw dataset is obtained by collecting 1000 images of objects with different rotation angles (563 occluded scenes), and these images are randomly masked in some regions. 800 images is used for training and the remaining 200 images for testing.

2) *Implementation Details*: Our experiments are carried out on a machine with two NVIDIA GeForce RTX 4090 GPUs. The number of epochs for training is set to 500, and the batch size is set to 2. We compare PDCNet with four single-shot state-of-the-art methods: FOA-Net [4], CTransU-Net [5], LightUNet [10], and PCTNet [6].

B. Qualitative Evaluation

The phase errors of different methods are shown in Fig. 7. We can observe that our method better integrates global structures in fringe images and local details in speckle images. To be specific, when only isolated objects are present in the non-occluded scenes, the performance of various methods shows little difference. In contrast, when objects overlap with each other in the occluded scenes, our method demonstrates better perceptual capabilities and shows strong adaptation power.

C. Quantitative Evaluation

In Table I, four metrics are used to quantitatively compare with other methods. Our method has excellent performance on all metrics, demonstrating that our PDCNet is suitable for various target categories, which indicates the effectiveness of our parallel dual-branch CNN-Transformer framework. Fig. 8 shows the performance of the different methods on the original test set and the occluded-only test set, and it can be seen that our method has a more obvious advantage on the latter.

D. Ablation Studies

1) *Effect of Different Architectures*. We verify the necessity of LTB and the HPB in the corresponding branch. The results are shown in Table II. In architecture a), we change LTB as HPB, that is, both the fringe and speckle features are extracted by HPB. Similarly, in architecture c), these features are both extracted by LTB. The results demonstrate that although the ability of feature extraction for HPB is stronger than that of LTB, it is still worse than that of our PDCNet which cooperates with HPB and LTB. In architecture b), we use HPB and LTB to extract fringe and speckle features respectively, and its effect is also worse than that of our method, which proves that the proposed architecture effectively leverages the advantages of both modalities.

2) *Effect of Hyperparameters*. Within our PDCNet, z_N in the combined loss function is a hyperparameter to balance the base loss and the auxiliary saliency-aware loss. As shown in Table III, extensive experiments show that the best performance when $z_N=0.8$. Moreover, we compare the effects of different depth configurations in Table IV. Let N_{LT} and N_{HP} indicate the repeating number of the LTB and the HPB in the corresponding branch respectively. We notice that simply increasing the depth would not always bring better performance. When the repeating number in each branch is set to 3, the localization error is minimal.

3) *Effect of DAAM*. We compare our DAAM with other lightweight attention modules, including the SE attention [39] and CBAM [40]. For other settings, we follow the original PDCNet. As shown in Table V, our DAAM consistently demonstrates superior performance across both the original and occluded-only test sets and exhibits more significantly superior results on the latter. Specifically, DAAM surpasses SE attention by an average of 13.93% on precision. We argue that the advantage benefits from essential location information, whereas SE attention only takes information between channels into account. Moreover, DAAM outperforms CBAM by an average of 10.67% on precision. We think this is because CBAM utilizes a convolutional layer to encode local spatial information while DAAM encodes global information with two complementary 1D global pooling operations, which enables our attention to capture long-range dependencies. These factors are the reason why our modules also perform well on the occluded-only test sets.

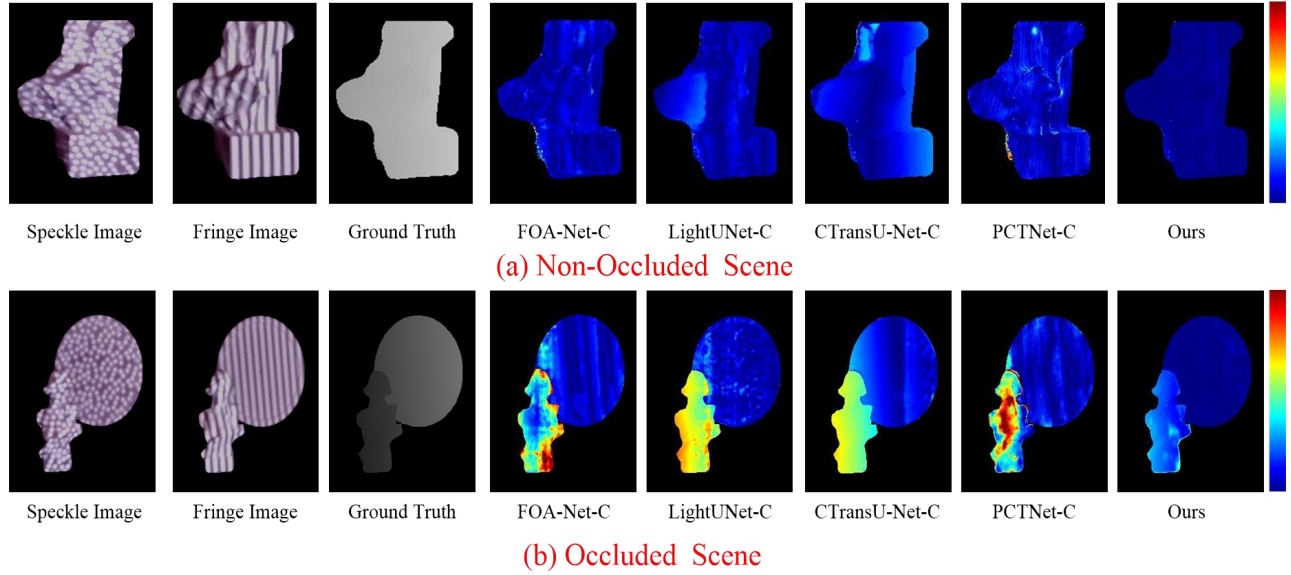


Fig. 4. Qualitative comparison results. The fourth column to the eighth column show the error maps obtained from different methods. The suffix C denotes the input is a concatenation of fringe images and the corresponding speckle images.

TABLE I

QUANTITATIVE RESULTS ON OUR DATASET. THE SUFFIX C DENOTES THE INPUT IS A CONCATENATION OF FRINGE IMAGES AND THE CORRESPONDING SPECKLE IMAGES.

Method	Framework	EPE	ERR3	ERR5	ERR10
FOA-Net	C	1.67	14.43	10.40	4.43
LightUNet	C	1.84	16.86	5.00	1.93
CTransU-Net	T	1.97	18.92	5.65	1.91
PCTNet	$C + T$	1.92	16.62	5.97	1.83
FOA-Net-C	C	1.36	9.47	6.01	3.53
LightUNet-C	C	1.39	10.28	6.33	1.67
CTransU-Net-C	T	1.42	13.45	4.93	1.94
PCTNet-C	$C + T$	1.37	9.71	5.27	1.70
PDCNet (Ours)	$C // T$	0.98	6.91	3.37	1.20

TABLE II
COMPARISON OF DIFFERENT ARCHITECTURES.

Architecture	Fringe / Speckle	EPE	ERR3	ERR5	ERR10
a)	CNN / CNN	1.23	8.63	4.90	1.18
b)	CNN / Trans	1.34	10.69	7.02	3.96
c)	Trans / Trans	1.27	8.81	4.57	2.13
d)	Trans / CNN (Ours)	0.98	6.91	3.37	1.20

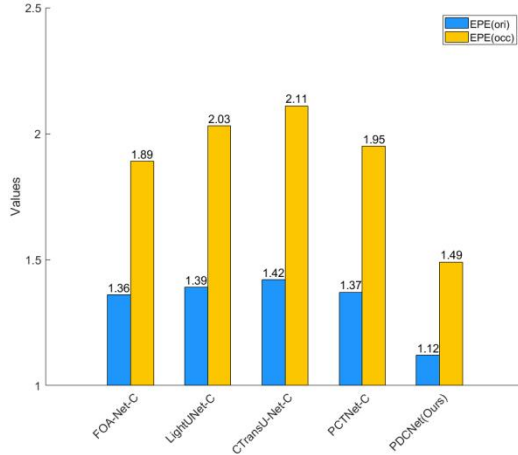


Fig. 8. Comparison of different methods on the original test set and the occluded-only test set.

TABLE III
COMPARISON OF DIFFERENT Z_N .

z_N	EPE	ERR3
0.5	1.21	7.83
0.6	1.20	7.96
0.7	1.13	7.12
0.8	0.98	6.91
0.9	1.15	7.06

TABLE IV
COMPARISON OF DIFFERENT DEPTH CONFIGURATIONS.

N_{LT}	N_{HP}	EPE
1	1	1.20
2	2	1.14
3	3	0.98
4	4	1.14
5	5	1.15

TABLE V

EVALUATION OF ATTENTION MECHANISMS ON THE ORIGINAL TEST SET AND THE OCCLUDED-ONLY TEST SET.

Mechanism	EPE (original)	EPE (occluded)
DAAM (Ours)	0.98	1.37
CBAM	1.06	1.59
SE	1.10	1.65

TABLE VI

EVALUATION OF SALIENCY-AWARE PATHS.

Path	EPE	ERR3
Ours	0.98	6.91
Ours-BT	1.18	7.64
Ours-BC	1.21	7.70
Ours-BT-BC	1.25	8.32

TABLE VII

EVALUATION OF DIFFERENT OUTPUT REPRESENTATIONS.

Head	EPE	ERR3	SEE
Regression	1.12	7.00	1.77
Unimodal	1.03	6.89	1.46
Adaptive Mixture	0.98	6.91	1.25

4) *Effect of Saliency-Aware Path.* Table VI shows the results after removing the saliency-aware path in the Transformer branch (denoted as BT) and CNN branch (denoted as BC). Despite this branch is used only during the training stage, it can lead to at least a 5.08% performance improvement. This scheme, which does not introduce additional costs during the inference stage, can also be applied to other tasks involving SL images.

5) *Effect of Adaptive Mixture Density Head.* The choice of output representation will directly affect the final performance. Therefore, we explore the impact of different representations in Table VII. In addition to EPE, we also evaluate the Soft Edge Error (SEE) metric on pixels belonging to boundaries [32].

V. CONCLUSION

In this paper, we propose an effective end-to-end dual-branch CNN-Transformer framework for 3D shape measurement. Specifically, we leverage the CNN branch to extract local information from speckle images and the Transformer to obtain global representations from fringe images. In addition, we design a double-stream attention aggregation module to integrate complementary features from different branches. An adaptive mixture density head with bimodal Gaussian distribution is used for learning a representation that is precise near discontinuities. Extensively comparative experiments reveal the advantage of PDCNet over state-of-the-art measurement algorithms in terms of qualitative and quantitative assessment.

REFERENCES

- [1] A. Marrygo, F. Gao, and S. Zhang, "State-of-the-art active optical techniques for three-dimensional surface metrology: a review," *J Opt Soc Am A*, 2020, 37(9), pp. 60-77.
- [2] K. Xu, H. Chen, C. Xu, Y. Jin, G. Zhu, "Structure-Texture Aware Network for Low-Light Image Enhancement," *IEEE Transactions on Circuits and Systems for Video Technology*, 2022.
- [3] X. Song and L. Wang, "Dual-stage hybrid network for single-shot fringe projection profilometry based on a phase-height model," *Optics Express*, 2024, pp. 891-906.
- [4] X. Guo, Y. Li, J. Qian, Y. Che, C. Zuo, Q. Chen, E. Lam, H. Wang, and S. Feng, "Unifying temporal phase unwrapping framework using deep learning," *Optics Express*, 2023, pp. 16659-16675.
- [5] G. Sun, B. Li, Z. Li, X. Wang, P. Cai, and C. Qie, "Phase unwrapping based on channel transformer U-Net for single-shot fringe projection profilometry," *Journal of Optics*, 2023.
- [6] X. Zhu, Z. Han, Z. Zhang, L. Song, H. Wang and Q. Guo, "PCTNet: depth estimation from single structured light image with a parallel CNN-transformer network," *Measurement Science and Technology*, 2023.
- [7] T. Li, G. Zhou, Y. Zhang, L. Fan, S. Zhang, and Q. Hao, "Single-shot absolute 3D measurement based on speckle-embedded fringe projection," *Optics and Lasers in Engineering*, 2024.
- [8] G. Riegler, Y. Liao, S. Donne, V. Koltun, and A. Geiger, "Connecting the dots: Learning representations for active monocular depth estimation," In *CVPR*, 2019, pp. 7624-7633.
- [9] J. Mohammad Mahdi, C. Camilla, and F. Francois. "DepthInSpace: Exploitation and Fusion of Multiple Video Frames for Structured-Light Depth Estimation," In *ICCV*, 2021.
- [10] H. Nguyen, T. Tran, Y. Wang, and Z. Wang, "Three-dimensional Shape Reconstruction from Single-shot Speckle Image Using Deep Convolutional Neural Networks," *Optics and Lasers in Engineering*, 2021.
- [11] Y. Zhang, S. Khamis, C. Rhemann, J. Valentin, A. Kowdle, V. Tankovich, M. Schoenberg, S. Izadi, T. Funkhouser, and Sean Fanello, "Activestereonet: End-to-end self-supervised learning for active stereo systems," In *ECCV*, 2018, pp. 784-801.
- [12] Y. Liu, W. Wang, X. Xu, X. Guo, G. Gong, and H. Lu, "Lightweight real-time stereo matching algorithm for AI chips," *Computer Communications*, 2023, pp. 210-217.
- [13] L. Wang, D. Lu, R. Qiu and J. Tao, "3D reconstruction from structured-light profilometry with dual-path hybrid network," *EURASIP Journal on Advances in Signal Processing*, 2022.
- [14] O. Ronneberger, P. Fischer, and T. Brox, "U-net: convolutional networks for biomedical image segmentation," In *International Conference on Medical Image Computing and Computer-Assisted Intervention*, 2015, pp. 234-241.
- [15] C. Zuo, L. Huang, M. Zhang, Q. Chen, and A. Asundi, "Temporal phase unwrapping algorithms for fringe projection profilometry: A comparative review," *Opt. Lasers Eng.* 2016, pp. 84-103.
- [16] W. Yin, Q. Chen, S. Feng, T. Tao, L. Huang, M. Trusiak, A. Asundi, and C. Zuo, "Temporal phase unwrapping using deep learning. *Scientific Reports*, 2019.
- [17] H. Yu, X. Chen, R. Huang, L. Bai, D. Zheng, and J. Han, "Untrained deep learning-based phase retrieval for fringe projection profilometry," *Optics and Lasers in Engineering*, 2023.
- [18] Y. Li, J. Qian, S. Feng, Q. Chen, and C. Zuo, "Deep-learning-enabled dual-frequency composite fringe projection profilometry for singleshot absolute 3D shape measurement," *Opto-Electron Adv.* 2022.
- [19] Z. Peng, W. Huang, S. Gu, L. Xie, Y. Wang, J. Jiao, Q. Ye, "Conformer: Local Features Coupling Global Representations for Visual Recognition," In *ICCV*, 2021, pp. 357-366.
- [20] Y. Chen, X. Dai, D. Chen, M. Liu, X. Dong, L. Yuan, and Z. Liu, "MobileFormer: Bridging MobileNet and Transformer," In *CVPR*, 2022, pp. 5260-5269.
- [21] A. Srinivas, T. Lin, N. Parmar, J. Shlens, P. Abbeel, and A. Vaswani, "Bottleneck transformers for visual recognition," In *CVPR*, 2021, pp. 16519-16529.
- [22] S. Ascoli, H. Touvron, M. Leavitt, A. Morcos, G. Biroli, and L. Sagun, "Convit: Improving vision transformers with soft convolutional inductive biases," In *ICML*, 2021, pp. 2286-2296.
- [23] A. Howard, M. Sandler, G. Chu, L. Chen, B. Chen, M. Tan, W. Wang, Y. Zhu, R. Pang, V. Vasudevan, Q. Le, and H. Adam, "Searching for mobilenetv3," In *ICCV*, 2019, pp. 2286-2296.
- [24] K. He, X. Zhang, S. Ren, and J. Sun, "Deep residual learning for image recognition," In *CVPR*, 2016, pp. 770-778.
- [25] T. Xiao, M. Singh, E. Mintun, T. Darrell, P. Dollar, and R. Girshick, "Early convolutions help transformers see better," *Advances in Neural Information Processing Systems*, 2021, pp. 30392-30400.
- [26] Z. Wu, Z. Liu, J. Lin, Y. Lin, and S. Han, "Lite transformer with long-short range attention," In *ICLR*, 2020.
- [27] X. Zhu, Z. Lei, X. Liu, H. Shi, and S. Li, "Face alignment across large poses: A 3d solution," In *CVPR*, 2016.
- [28] A. Kumar and R. Chellappa, "Disentangling 3d pose in a dendritic cnn for unconstrained 2d face alignment," In *CVPR*, 2018.
- [29] D. Eigen and R. Fergus, "Predicting depth, surface normals and semantic labels with a common multi-scale convolutional architecture," In *ICCV*, 2015, pp. 2650-2658.
- [30] Q. Hou, D. Zhou, and J. Feng, "Coordinate attention for efficient mobile network design," In *CVPR*, 2021, pp. 13713-13722.
- [31] F. Chollet, "Xception: deep learning with depthwise separable convolutions," In *CVPR*, 2017, pp. 1251-1258.
- [32] F. Tosi, Y. Liao, C. Schmitt, and A. Geiger. "SMD-Nets: Stereo Mixture Density Networks," In *CVPR*, 2021.
- [33] C. Gu, Y. Zhao, and C. Zhang. "Learning to predict diverse human motions from a single image via mixture density networks," *Knowledge-Based Systems*, 2022.
- [34] S. Choi, K. Lee, S. Lim, and S. Oh, "Uncertainty-aware learning from demonstration using mixture density networks with sampling-free variance modeling," in *IEEE International Conference on Robotics and Automation*, 2018, pp. 6915-6922.
- [35] Y. He and J. Wang, "Deep Mixture Density Network for Probabilistic Object Detection," *IEEE/RSJ International Conference on Intelligent Robots and Systems*, 2020.
- [36] Z. Chen, Q. Xu, R. Cong, and Q. Huang, "Global Context-Aware Progressive Aggregation Network for Salient Object Detection," In *AAAI*, 2020, pp. 10599-10606.
- [37] Q. Zhang, X. Su, L. Xiang, and X. Sun, "3-D shape measurement based on complementary gray-code light," *Opt. Lasers Eng.* 2012, 50(4), pp. 574-579.
- [38] S. Yu, T. Gong, H. Wu, X. Sun, Y. Zhao, S. Wu, and X. Yu, "3D shape measurement based on the unequal-period combination of shifting Gray code and dual-frequency phase-shifting fringes," *Optics Communications*, 2022.
- [39] J. Hu, L. Shen, and G. Sun, "Squeeze-and-excitation networks," In *CVPR*, 2018, pp. 7132-7141.
- [40] S. Woo, J. Park, J. Lee, and I. Kweon, "Cbam: Convolutional block attention module," In *ECCV*, 2018, pp. 3-19.
- [41] L. Tang, J. Yuan, H. Zhang, X. Jiang, and Jiayi Ma, "Piafusion: A progressive infrared and visible image fusion network based on illumination aware," *Inf. Fusion*, 2022, pp. 79-92.
- [42] J. Ma, L. Tang, F. Fan, J. Huang, X. Mei, and Y. Ma, "Swinfusion: Cross-domain long-range learning for general image fusion via swin transformer," *IEEE CAA J. Autom. Sinica*, 2022, pp. 1200-1217.
- [43] J. Liu, X. Fan, Z. Huang, G. Wu, R. Liu, W. Zhong, and Z. Luo, "Target-aware dual adversarial learning and a multi-scenario multi-modality benchmark to fuse infrared and visible for object detection," In *CVPR*, 2022, pp. 5792-5801.

- [44] Z. Wang, Y. Chen, W. Shao, H. Li, L. Zhang. "SwinFuse: A residual swin transformer fusion network for infrared and visible images," *IEEE Transactions on Instrumentation and Measurement*, 2022.
- [45] H. Xu, J. Ma, J. Jiang, X. Guo, and H. Ling, "U2fusion: A unified unsupervised image fusion network," *IEEE TPAMI*, 2022, pp. 502-518.